Integration of 3D Rogowski sensor within power module

Guillaume Viné, Paul-Etienne Vidal, Philippe Lasserre, Julie Tarrieu, Stéphane Baffreau

Integration of 3D Rogowski sensor within power module

Guillaume Viné
Laboratoire Génie de Production,
University of Technology of Tarbes
Toulouse University
Tarbes France
guillaum.vine@uttop.fr

Paul-Etienne Vidal
Laboratoire Génie de Production,
University of Technology of Tarbes
Toulouse University
Tarbes, France
paul-etienne.vidal@uttop.fr

Philippe Lasserre
DEEPConcept
Pau, France
philippe.lasserre@deepconcept.fr

Julie Tarrieu
DEEPConcept
Pau, France
julie.tarrieu@deepconcept.fr

Stéphane Baffreau
Laboratoire Génie de Production,
University of Technology of Tarbes
Toulouse University
Tarbes, France
stephane.baffreau@uttop.fr

***Abstract*—This study deals with the integration of Rogowski sensor into power module using 3D printing for the coil former and the custom-designed casing. The sensor design is done considering the fundamental constraints of Rogowski sensors and specific integration requirements. The sensor fabrication process is described, and performance tests are presented. Finally, measurements taken on a double-pulse test bench are discussed, highlighting the designed sensor ability to measure currents into medium/high power modules on wide frequency bandwidth.**

Keywords—power electronics, power module, integration, rogowski current sensor, 3D printing

I. INTRODUCTION

Ongoing advancements in power electronics, as wide bandgap components, 3D printing and smart gate drivers, are allowing power modules operating at higher frequencies, power densities, and compactness, with enhanced switching control and health monitoring. These advancements are accompanied by the need of sensors as close as possible to the power module. Regarding current measurement, the literature has emphasized the use of PCB Rogowski sensors embedded [1] onto the power module for both switching and phase current [2]. Such a sensor can deserve several purposes, as usual AC current measurement [3] and short circuit detection [4]. It is usual to design PCB based Rogowski sensors. The PCB based design eases the integration purpose [5]. In this paper, the power module integration of a Rogowski dedicated sensor is introduced. A housing 3D printing of the sensor coil, as well as for the power module casing is developed to reach sensor specifications. Both, integration and measurement's performance are targeted. The integration process and wide frequency bandwidth characterization are applied to the phase current measurement for medium/high power application.

II. FUNDAMENTALS FOR SENSOR DESIGN

A. Rogowski sensor

As illustrated in Fig.1 the Rogowski sensor corresponds to a wounded coil placed around a primary conductor. The primary current I_p induces an electromotive force e proportional to the temporal variation of I_p. The Rogowski coil is associated with a return conductor and integrator circuit resulting in the output voltage V_{out} of the Rogowski sensor being ideally proportional to the primary current I_p.

This results in eq.1, where p is the Laplace operator, M_c is the mutual inductance between the primary conductor and the coil, and G_I is the integrator gain:

$$\mathrm{V_{out}(p) = M_c * p * I_p(p) * \frac{G_I}{p} = M_C * I_p(p) * G_I} \qquad (1)$$

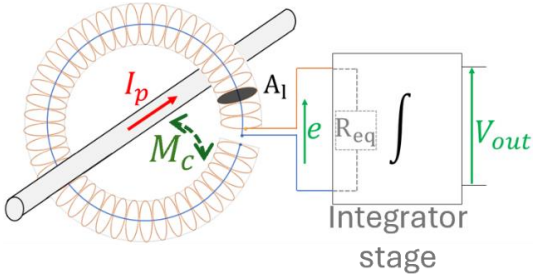

Fig.1. Rogowski sensor system

Nevertheless, the expected ideal behavior described in eq. 1 is influenced by the actual geometry of the coil, its associated parasitic elements, the integrator topology, component values, and environmental constraints. Indeed, the related challenges are listed in the following.

B. Design challenges and trade-offs

The performance of a Rogowski sensor involves a complex trade-off among various parameters [6]. In this context, we will focus on the following key aspects to guide the design: low and high frequency cut-off, sensitivity, and intrinsic noise. The main specification targets are a bandwidth from 1 Hz to 10 MHz along with a sensitivity of 1 mV/A. Both the coil design and the integrator circuit significantly influence these characteristics. Let us explore their respective contributions.

1) Coil design

Despite the ideal assumption of Rogowski coil behavior, the intrinsic RLC parasitic elements of the coil affect performance parameters, particularly sensitivity and high-frequency cut-off. In this context, the coil can be represented as an equivalent RLC circuit, as illustrated in Fig.2, where R_c, L_c, C_c , being the equivalent resistive, inductive and capacitor values, respectively.

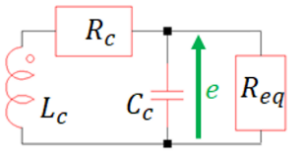

Fig.2. Rogowski sensor coil model

Considering at a first stage the integrator circuit as its input equivalent resistance R_{eq}, the transfer function of the coil $F_{coil}(p)$ is expressed in eq.2. Parameters $[\alpha, \xi, f_0]$ are related to the parasitic elements $[R_c, L_c, C_c]$ as detailed in eq.3.

$$F_{coil}(p) = \frac{e(p)}{Ip(p)} = \frac{\alpha}{1+\frac{2*\xi}{2\pi f_0}*p+\frac{p^2}{(2\pi f_0)^2}} * M_c * p \quad (2)$$

$$\begin{cases} \alpha = \frac{R_{eq}}{R_c+R_{eq}} \\ f_0 = \frac{1}{2\pi}\sqrt{\frac{\alpha}{L_c C_c}} \\ \xi = \frac{L_c*2\pi f_0}{2*R_{eq}} \end{cases} \quad (3)$$

$F_{coil}(p)$ illustrates the relations between coil design, R_{eq}, and the system high cut-off frequency denoted f_H. From one hand, the coil ohmic resistance R_c, impacts its high-frequency gain due to skin effect in the coil conductor. That results in the first design criterion of eq.4. On the other hand, damping ratio ξ must exceed 1 to overdamp the coil. In this case, f_H is linked to L_c and R_{eq} resulting in second design criterion of eq.4. These conditions on R_c and L_c significantly influence the coil's dimensions.

$$\begin{aligned} &\textit{First criterion:} && R_{eq} \gg R_c \\ &\textit{Second criterion:} && \frac{f_0}{2} > \frac{R_{eq}}{2\pi*L_c} = f_H \end{aligned} \quad (4)$$

Especially, to further understand the impact of the second criterion on the design, consider the well-known approximations for M_c and L_c , given in eq.5, where N_l is the number of loops and A_l is the loop area.

$$L_c = N_l * M_c = \mu_0 * N_l^2 * A_l \quad (5)$$

Since L_c is linked to the mutual inductance between the primary conductor and the coil as given in eq.5, and therefore to the Rogowski coil's gain as described in eq.1, the design must strike a balance between sensitivity and frequency bandwidth. The quadratic dependence of N_l on L_c and a linear dependence of A_l, underscores the interest of increasing the loop surface area rather than the loop number. This is the main argument in favor of 3D printing over most common PCB based and planar technology.

2) Integrator Circuit

As for the coil design, the integrator circuit plays a critical role onto the overall sensor performance. To achieve a wide frequency band for the Rogowski sensor, on the order of 1 Hz to 10 MHz, the chosen integrator topology is the non-inverting integrator circuit, as shown in Fig.3.

The non-inverting integrator circuit offers over the inverting one to be limited in high frequency only by the op-amp, and allowing a better input-output decoupling, [7].

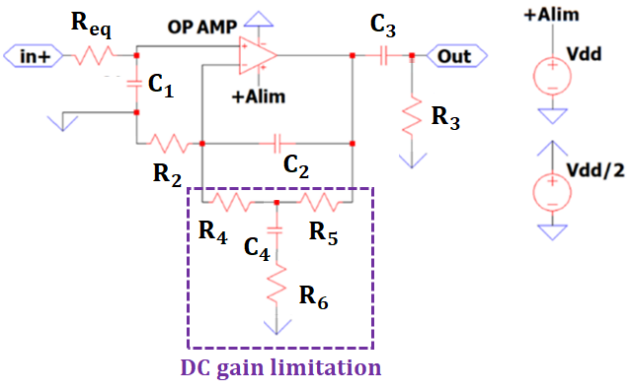

Fig.3. Non-inverting integrator topology

In this topology, the integration is carried out at low frequency by the RC filter $\{R_{eq}, C_1\}$ and at high frequency by the op-amp associated to the RC filter $\{R_2, C_2\}$. This based on the precise matching between the time constants $R_{eq} * C_1$ and $R_2 * C_2$ which constitutes a drawback considering the uncertainty in capacitor component values: usually ranging from 5% to 10%. Indeed, a tunable series resistance with R_{eq} can be added. While not considered in the initial demonstrator, this constraint impacts the results as will be highlighted in section IV. However, considering this matching, the integrator gain is express eq.6.

$$G_I = \frac{1}{R_{eq}*C_1} \quad (6)$$

Associated to eq.1, the sensitivity of the measurement system is so:

$$S_m = \frac{M_c}{R_{eq}*C_1} \quad (7)$$

The integrator's DC output is managed in three ways. Firstly, the DC gain limitation block allows to prevent output saturation. Secondly, the additional RC filter $\{R_4\ C_3\}$ further suppresses any remaining DC offset at the output of the circuit. Thirdly, the matching between R_{eq} and R_2 allows to suppress the contribution of the op-amp's differential input DC current. This matching between R_{eq} and R_2 also involves corresponding matching between C_1 and C_2 as their associated time constants must align.

However, the DC gain limitation block associated to C_2 forms a high-pass filter, as does $\{R_4\ C_3\}$. The time constants of these filters must be sufficiently high to achieve the desired low-frequency cut-off for the Rogowski sensor Notably, the inclusion of the DC gain limitation block represents an enhancement over the use of a single resistor, optimizing the balance between the constraints of DC output voltage and the low frequency cut-off performance of the integrator, as discussed in [8].

C. Rogowski design process

The design of the non-inverting integrator encompasses the following design process based on a previous design and simulation of the coil.

- Firstly, the resistor R_{eq} is selected to achieve the desired high-frequency cut-off, which is determined by the coil's inductance and the criteria established in eq.4. R_2 is so fixed.

- Secondly, the capacitor C_1 is dimensioned to ensure the required sensitivity, on the order of 1 mV/A. which is determined by the coil's mutual inductance and the calculated value of R_{eq}, based on eq.7. C_2 is fixed accordingly.
- The resistors R_3 and R_4, along with capacitor C_3 are set to achieve the targeted low-frequency cut-off while maximizing the suppression of any DC offset.
- The op-amp reference is selected considering its performance in terms of gain–bandwidth product, noise level and input DC offset.

In order to converge towards desired performances, this process has to be looped from coil design and simulation to integrator design and simulation. It has to be noted that the design of the coil is primarily focusing on the integration constraint due to the target power module.

III. Design, Fabrication and Integration

A. Integrated Rogowski coil design

Within the targeted application, the integration of Rogowski sensor is constrained by the allocated space within the power module package. The custom power module is a half-bridge SiC 3300V-500A, Fig.4. The allocated coil space is set to take into account the dielectric isolation to high voltage potentials. The insulation is provided thanks to the custom casing, resulting in the coil dimensions provided in Fig.5. The external dimensions of the coil are 76.6 mm x 13.5 mm x 8 mm, with rectangular loop area of 36 mm^2 and a pitch of 1.5 mm between loops, resulting in a total of 106 turns. The winding is done using a thin wire with a diameter of 0.255 mm.

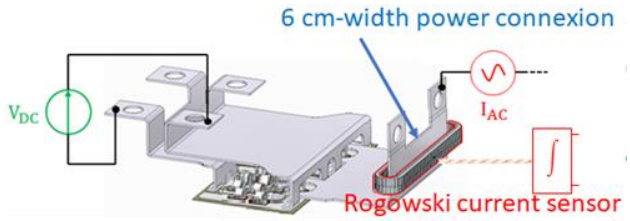

Fig.4. Power module sensor integration

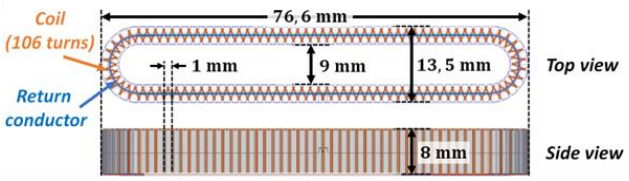

Fig.5. Detailed coil design

B. Coil simulation

The model and the simulation of the coil design was performed using Q3D extractor software. Consequently, the equivalent RLC parameters of the designed coil is extracted. The computed results are reported in Tab.1.

TAB.1. Equivalent electric parameters of the coil

L_c	M_c	R_c @10 MHz
2.05 µH	15 nH	3 Ω

As explained, these values are essential to determine the components value of the integrator, which is the aim of the next step. The calculation of the equivalent capacitor of the coil C_c is not address here as its influence on performance will be evaluated experimentally. C_c contributes to the high-frequency resonance of the coil.

C. Integrator circuitry design and simulation

The Rogowski sensor model is implemented on the SPICE simulator software LTspice as reported on Fig.6. It includes the Rogowski coil model, the integrator circuit and the symmetric power supply circuit for the op-amp.

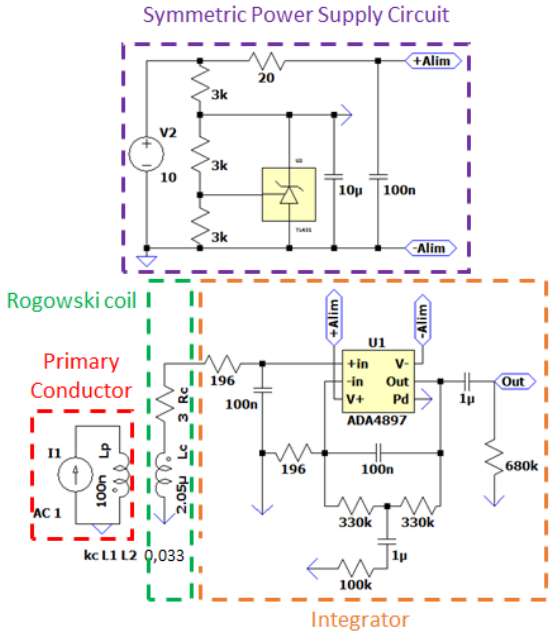

Fig.6. Rogowski sensor simulation.

Based on the design process detailed in section II.C, the component values of the integrator are determined and reported in Tab.2.

TAB.2. Integrator components

Component values			
R_{eq}	196 Ω	R_2	196 Ω
R_3	680 $k\Omega$	R_4	330 $k\Omega$
R_5	330 $k\Omega$	R_6	100 $k\Omega$
C_1	100 nF	C_2	100 nF
C_3	1 μF	C_4	1 μF
Op-amp ADA48976-1			
Gain-Bandwidth Product 90 MHz		Input Offset Voltage ±0.5 mV	Noise 1 nV/ √ Hz 2.8 pA/ √ Hz

As depicted in Fig.7 the simulation of the circuit highlights a linear behavior from 0.95 Hz to 16 MHz. Within these boundaries, the sensitivity is 0.87 mA/V with a change lower than 3 dB.

With a target sensitivity of 1 mV/A and a bandwidth of 1 Hz to 10 MHz, the results obtained show a slightly lower sensitivity and a higher bandwidth. Obviously, a minor redesign of the coil and adjustments to the integrator's

component values would allow to fit it. However, to validate the simulation and assess the overall performance of the integrated Rogowski sensor, fabrication and experimental testing will be conducted on this prototype.

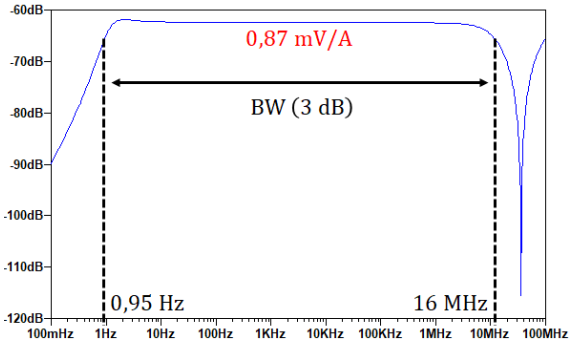

Fig.7. Performance simulation of the integrator circuit

D. Rogowoski sensor fabrication

The coil former is fabricated, by Stereolithography 3D printing, in 2 parts enabling the return conductor to be placed between them before assembly and manually wounding of the coil wire. The coil and the integrator circuit are shown Fig.8.a. The casing integration for both sensor and circuitry, is presented in Fig.8.b. The Rogowski sensor is surrounding the 6 cm width copper track. The track is the interconnexion that is used to be connected to voltage source potential.

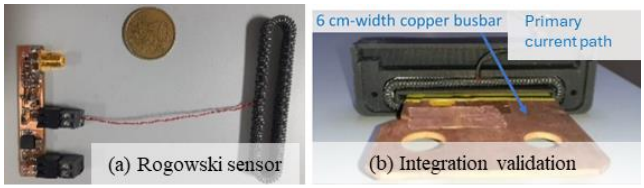

Fig.8. Complete Rogowski sensor realized

IV. PERFORMANCE AND VALIDATION TESTS

The experimental test and validation of the Rogowski sensor is achieved by a step-by-step process starting from standalone coil impedances, self and mutual, validation to the bandwidth and sensitivity validation.

A. Validation of coil impedances

The fabricated Rogowski coil is characterized using S-parameters to validate its impedance model and ensure compliance with the defined specifications in section II.B. S-parameter measurements are performed with a vector network analyzer in a test setup that includes the Rogowski coil associated to a representative primary conductor - a 6 cm-wide copper busbar - and a dedicated test card as illustrated in the measurement setup in Fig.9.

In this two-port S-parameter measurement, the primary conductor is connected to port 1, and the Rogowski coil to port 2. This configuration enables the determination of the coil's self-impedance Z_{coil} and the mutual impedance Z_{Mut} between the primary conductor and the Rogowski coil, according to the eq.8 and eq.9.

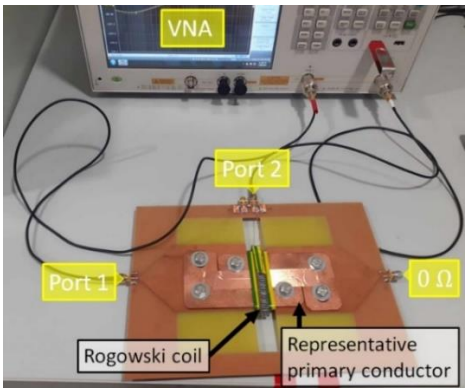

Fig.9. S-parameters Rogowski coil characterization set-up

In this two-port S-parameter measurement, the primary conductor is connected to port 1, and the Rogowski coil to port 2. This configuration enables the determination of the coil's self-impedance Z_{coil} and the mutual impedance Z_{Mut} between the primary conductor and the Rogowski coil, according to the following equations:

$$Z_{Coil} = \frac{(1+S_{11})*(1-S_{22})+S_{12}*S_{21}}{(1-S_{11})*(1-S_{22})-S_{12}*S_{21}} * 50\ \Omega \qquad (8)$$

$$Z_{Mut} = \frac{2*S_{21}}{(1-S_{11})*(1-S_{22})-S_{12}*S_{21}} * 50\ \Omega \qquad (9)$$

The imaginary part of the self-impedance, shown in Fig. 10.a, confirms that the coil design achieves a high-frequency bandwidth exceeding $10\ MHz$, in accordance with eq.2. Specifically, the high-frequency cut-off f_H is identified at $12\ MHz$, while the resonant frequency f_0 is higher than twice f_H. The real part of the self-impedance, depicted in Fig.10.b, verifies compliance with eq.3, using an equivalent resistance $R_{eq} = 196\ \Omega$, for the integrator, as determined in section III.C. Indeed, the real part of the self-impedance remains significantly lower than R_{eq} until $10\ MHz$. The magnitude of the mutual impedance is directly related to the mutual inductance M_c below $10\ MHz$, M_c is extracted as $18.8\ nH$, as shown in Fig.10.c.

The measured electrical parameters of the Rogowski coil are higher of approximately 25% than the simulated values for the resistance and inductances. This discrepancy is attributed to the non-rectangular shape of the loops, which exhibit a significant radius of curvature, resulting in increased wire length and larger loop surfaces. This represents an area for improvement in the simulation to accurately guide the design.

However, it has to be noted an increase in sensitivity, aligning well with the target value of 1 mV/A goal. Indeed, the re-simulation of the circuit, incorporating these measured values for the Rogowski sensor's electrical model, yields a sensitivity of 1.09 mV/A.

B. Testing of intrinsic noise of the integrator

The coil is connected to the integrator, as shown in Fig.8, to evaluate the overall performance of the sensor. The first objective is to characterize the integrator's output noise with no current flowing through the coil. This provides the sensor's absolute accuracy in measuring low currents. The output noise of the designed sensor is measured and compared to a commercial sensor, CWT6R.

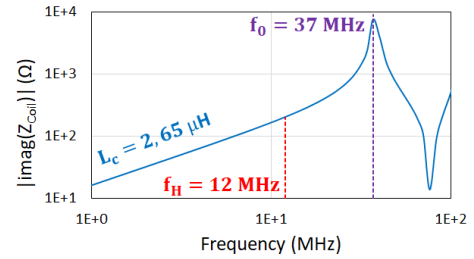

(a) Imaginary part of coil self-impedance

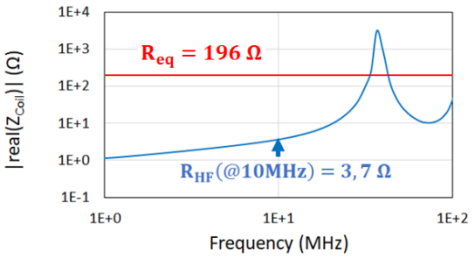

(b) Real part of coil self-impedance

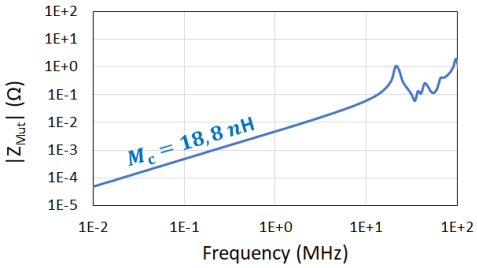

(c) Magnitude of the mutual impedance between the primary conductor and the coil

Fig.10. Self and Mutal impedances of the Rogowski coil

The noise curves, shown in Fig. 11, were generated using the Fast Fourier Transform of the sensor output voltages over a 1-second time window. These curves were adjusted according to the sensors' sensitivities: 1.09 mV/A for the designed sensor and 5 mV/A for the commercial one.

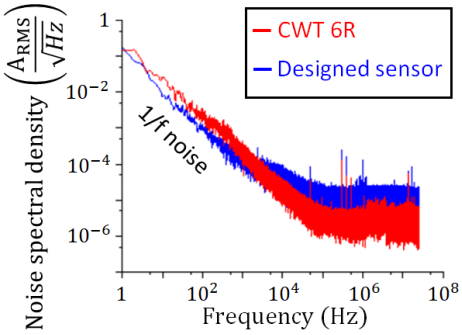

Fig.11. Internal noise measurement of the designed Rogowski sensor

The designed sensor demonstrates good noise performance compared to the commercial one, particularly at low frequencies where the integrator's intrinsic output noise is at its peak. This noise originates from the op-amp, which generates significant low-frequency noise due to its 1/f characteristic. The output noise is closely tied to the op-amp's intrinsic performance, including its voltage and current input noise, as well as the input impedances and integrator gain. The use of the ultra-low noise op-amp ADA48976-1 justifies the sensor's excellent performance.

C. Sensitivity and Bandwidth test of the Rogowski sensor

The sensitivity of the Rogowski sensor is measured using a function generator with 50 Ω impedance, swept in frequency, connected to multi-turn primary conductors, ensuring the induced voltage to exceed the output noise produced by the op-amp. The test-bench is presented in Fig.12. The measurements were conducted in two frequency bands. In the first band, from 0.2 Hz to 400 Hz, where op-amp noise is relatively high, a 100-turn primary conductor was used to provide sufficient equivalent current through the sensor. In the second band, from 400 Hz to 20 MHz, a 7-turn conductor was sufficient. For high frequencies, it is crucial to limit the number of turns to prevent excessive multi-turn inductance, which could restrict the primary current. The measurements are compared with commercial probes: a CWT 6R for the first band and a CWT 50mini for the second band, both offering adequate bandwidths.

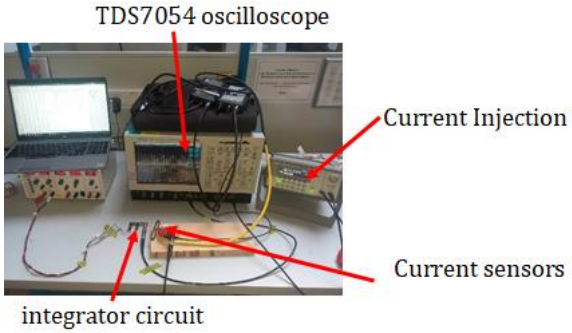

Fig.12. Sensitivity/Bandwidth measurement set-up

As stated in Fig.13, the sensitivity is 1.095 mV/A, very close to the calculated one in section IV.A. The wide frequency bandwidth where the linear behavior is ensured, within 1.15 Hz to 8.5 MHz. The sensitivity and the cut-off frequencies are close to the intended design values stated in III.C.

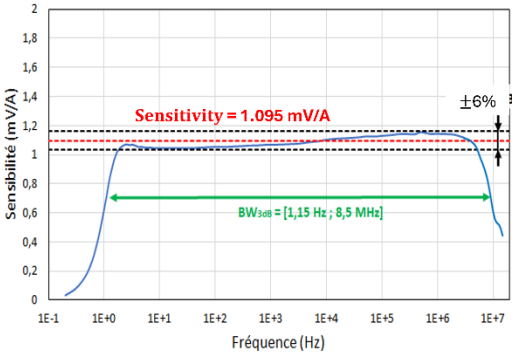

Fig.13. Sensitivity/Bandwidth measurement of the Rogowski sensor

Let us remark that the non-constant sensitivity is a limit of the integrator design. This is caused by the mismatch between the capacitors C_1 and C_2 exhibit a discrepancy in their values: C_1 was measured at 95 nF and C_2 was measured at 105 nF. To overcome this limitation, a tunable resistor can be added in series with R_{eq} to fine-tune the matching between $\{R_{eq}, C_1\}$ and $\{R_2, C_2\}$.

D. Double-Pulse test

Finally, the Rogowski sensor is tested along with a double pulse test bench 1200 V-500 A. The test bench is presented in Fig.14. The switching is produced by the lower

MOSFET of Half-bridge architecture. The double pulse consists of charging an inductance L_{ch}, during a given time, followed by two consecutives OFF and ON control applied to the lower switch. Indeed, both nominal voltage and current values can be switched.

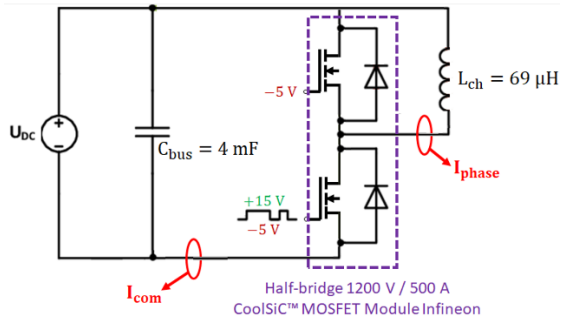

(a) Schematic

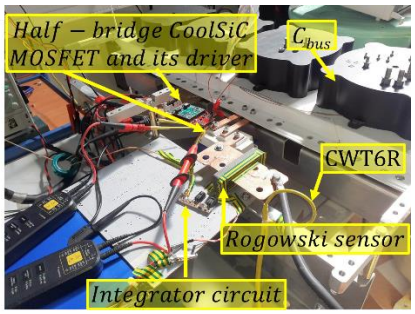

(b) Test bench

Fig.14. Double pulse test bench

In our case study, the Rogowski sensor is measuring different currents. Firstly, the phase current I_{phase} and secondly the lower switch current I_{com} . The current measured is flowing through a 6 cm copper tracks, acting as the primary winding. The measurement results are compared to CWT6R Rogowski commercial sensor. The CWT6R acts as a reference. Firstly, the phase current is measured @ 500 A, Fig. 15. The transient behavior is in good agreement, whereas during the steady state establishment, our solution varies slightly. It is attributed to the sensitivity change explained in section IV.C. Secondly, the high di/dt switching current is also monitored @ 180 A as illustrated in Fig.16 and Fig.17. The sensor shows a very good agreement in fast transient measurement. As a conclusion, it is noted that the comparison with the CWT6R sensor revealed a good agreement in the frequency bandwidth and some differences in very low-frequency phase current.

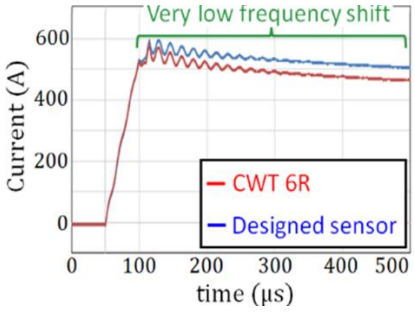

Fig.15. Phase current measurement during double pulse test

.

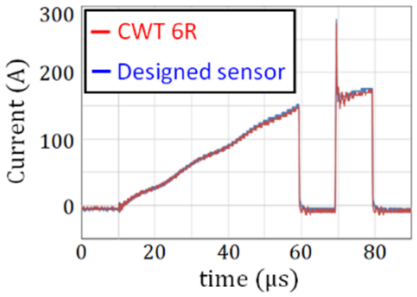

Fig.16. Switching current measurement I_{com} during double pulse test

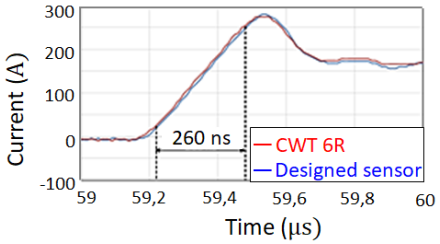

Fig.17. Zoom on the current measurement of the MOSFET turn-on switch

V. Conclusions and Future Work

The integration of a 3D Rogowski sensor within medium/high power module has been studied. The feasibility has been demonstrated based on 3D printing fabrication of the coil former and custom casing. The design and testing methodology were described, resulting in a sensor that nearly meets specified performance, with identified design improvements. Future work will address common mode immunity related to very high dv/dt constraints, major constraints of the Rogowski sensor technology. Enhancements could include shielding and the implementation of differential Rogowski coil topologies.

References

[1] T. Funk et al. “A Fully Integrated DC to 75MHz Current Sensing Circuit with On-Chip Rogowski Coil”, 38th IAS Annual Meeting on Conference Record of the Industry Applications Conference, 2003. 12-16 Oct. DOI: 10.1109/IAS.2003.1257710

[2] S. Mocevic et al., "Phase Current Sensor and Short-Circuit Detection based on Rogowski Coils Integrated on Gate Driver for 1.2 kV SiC MOSFET Half-Bridge Module," 2018 IEEE Energy Conversion Congress and Exposition (ECCE), Portland, OR, USA, 2018.

[3] E. Abdi-Jalebi et al. “High-Performance Low-Cost Rogowski Transducers and Accompanying Circuitry”, IEEE Transactions on instrumentation and measurement, Vol. 56, N°. 3, June 2007.

[4] S. Mocevic et al., “Comparison and Discussion on Shortcircuit Protections for Silicon-Carbide MOSFET Modules: Desaturation Versus Rogowski Switch-Current Sensor” IEEE Transactions on Industry Applications, Vol. 56, N°. 3, May/June 2020.

[5] J. Wang et al. "Integrated switch current sensor for shortcircuit protection and current control of 1.7-kV SiC MOSFET modules," 2016 IEEE Energy Conversion Congress and Exposition (ECCE), Milwaukee, WI, USA, 2016, pp. 1-7, doi: 10.1109/ECCE.2016.7855210

[6] W. Zhang et al, “High-Bandwidth Combinational Rogowski Coil for SiC MOSFET Power Module”, IEEE Transactions on power electronics, Vol. 37, N°. 4, April 2022

[7] H. Votzi et al. "Low-cost current sensor for power capacitors based on a PCB Rogowski-coil." Proceedings of International Exhibition and Conference for Power Electronics, Intelligent Motion and Power Quality (PCIM Europe). 2011.

[8] L. Ming et al, "Integrator Design of the Rogowski Current Sensor for Detecting Fast Switch Current of SiC Devices," 2019 IEEE Energy Conversion Congress and Exposition (ECCE), Baltimore, USA, pp. 4551-4557, doi: 10.1109/ECCE.2019.8911874